



RESEARCH ARTICLE OPEN ACCESS

Breathing-Induced Airflow Measurements at Multiple Positions in a 3D-Printed Nasal Cavity

Kota Shiba¹  | Kayoko Saito¹ | Masayoshi Tei² | Nagomi Yonezawa² | Rumi Sekine²  | Monami Nagai² | Hirotaka Tanaka² | Yuji Kishimoto² | Ryo Tamura^{3,4} | Genki Yoshikawa^{1,5} | Nobuyoshi Otori² | Eri Mori²

¹Research Center for Macromolecules and Biomaterials (RCMB), National Institute for Materials Science (NIMS), Tsukuba, Ibaraki, Japan | ²Department of Otorhinolaryngology, The Jikei University School of Medicine, Tokyo, Japan | ³Center for Basic Research on Materials, National Institute for Materials Science (NIMS), Tsukuba, Ibaraki, Japan | ⁴Graduate School of Frontier Sciences, The University of Tokyo, Kashiwa, Chiba, Japan | ⁵Materials Science and Engineering, Graduate School of Pure and Applied Science, University of Tsukuba, Tsukuba, Ibaraki, Japan

Correspondence: Kota Shiba (shiba.kota@nims.go.jp) | Eri Mori (mori.eri@jikei.ac.jp)

Received: 13 February 2026 | **Revised:** 11 May 2026 | **Accepted:** 15 May 2026

Keywords: 3D printing | airflow | fluid dynamics | nasal cavity | pressure differential | rhinomanometry

ABSTRACT

Evaluating nasal cavity airflow is crucial in both fundamental science and clinical settings. While rhinomanometry (RM) effectively assesses global nasal resistance, developing alternative methods for detailed local structural evaluation remains challenging. Here, we report an approach to measure local pressure at multiple positions in the nasal cavity using 3D-printed models created based on computed tomography data of five healthy individuals. This approach records multiple pressure differential values at arbitrary positions in the nasal cavity during a breathing-like inhalation/exhalation cycle. The measured data are unique to the corresponding individuals and correlate well with the RM results from human-assisted breathing using the 3D-printed models. Our experimental approach will open up possibilities for a deeper understanding of the relationship between fluid dynamics in the nasal cavity and practical air flow in the nasal cavity.

1 | Introduction

Breathing is essential for humans, enabling both pulmonary gas exchange and olfactory perception. During breathing, sniffing, or other inhalation/exhalation-processes, air flows through the nasal cavity—a complex structure that significantly influences airflow dynamics—and poses challenges for experimental investigation. Currently, rhinomanometry (RM) is widely used to provide an objective pressure-flow assessment of nasal patency and to quantify global nasal airway resistance [1–10]. However, because the measurement is inherently lumped over the entire nasal passage, it does not directly resolve where pressure losses occur or how local anatomical features shape the intranasal flow distribution. The inherent limitation of RM, which lumps measurements over the entire nasal passage, often leads to clinical inconsistencies, such as the paradoxical sensation of

nasal obstruction, even with a seemingly patent airway [11, 12]. While computational fluid dynamics (CFD) simulations offer a powerful alternative by providing spatially resolved predictions of intranasal flow and transport [13–18], its quantitative outcomes can be sensitive to modeling choices and uncertainties in patient-specific geometry reconstruction from computed tomography (CT) images [19, 20]. Moreover, the development of CFD as a reliable, patient-specific decision-support tool is constrained by the scarcity of spatially resolved validation data within the nasal cavity [21, 22]. In this context, there is a clear need for an experimental approach that enables direct, localized measurements of nasal airflow dynamics while preserving subject-specific anatomy. Unlike RM and CFD, position-specific pressure measurements within the nasal cavity have remained largely unexplored. As only a few previous studies have demonstrated local pressure measurements in the nasal cavity [23, 24], devel-

This is an open access article under the terms of the [Creative Commons Attribution](https://creativecommons.org/licenses/by/4.0/) License, which permits use, distribution and reproduction in any medium, provided the original work is properly cited.

© 2026 The Author(s). *Advanced Sensor Research* published by Wiley-VCH GmbH

oping such an approach would provide crucial validation data for CFD and deepen our understanding of the relationship between airflow, nasal structure, and physiological sensations such as olfaction.

In this study, we described an approach for measuring local pressure in the nasal cavity using 3D-printed nasal cavity models. We employed commercial pressure differential sensors to measure pressure differential values during breathing-mimicked inhalation/exhalation cycles at various flow rates. We inserted these sensors into the 3D-printed models through holes created at multiple positions to gather detailed site-specific information. We also performed RM measurements using the same 3D-printed models and compared the results with the sensor-based values to demonstrate the validity and discussed the potential application of our experimental approach.

2 | Methods and Materials

2.1 | Reconstruction and 3D Printing of Nasal Cavity Models

The first step in our approach involves the precise fabrication of person-specific nasal cavity models. In this cross-sectional study, we recruited five healthy individuals (denoted as Ind. 1–5) and used CT (3D Accuitomo, J. MORITA MFG. CORP.) to acquire the nasal cavity data for 3D printing. The CT data's voxel size (dissection to dissection distance) was 0.25 mm. The 3D printer (Agilista, KEYENCE Corp.) offered high resolution (635 dpi \times 400 dpi lateral, 0.015 mm vertical), ensuring accurate reproduction of the nasal cavity's complex structure. Each CT dataset in Digital Imaging and Communications in Medicine (DICOM) format was edited using commercial software (TomoShop Viewer, Systemcreate Co., Ltd.) to open 12 through-holes (both the right and left noses had six through-holes) for sensor insertion, as shown in Figure 1a. The holes of the right and the left nose were in the same position. The 12 through-holes for pressure sensors were standardized across all subjects by targeting key anatomical regions: the inferior meatus, the middle meatus, the nasal floor, and the olfactory cleft. We chose these locations to represent the primary airflow pathways and clinically significant areas. The holes were created with consistency for all five individuals. First, the holes for the middle meatus were created where the natural ostium of the maxillary sinus is located. Second, the holes for the inferior meatus, the nasal floor, and the middle part of olfactory cleft were created on the same coronal plane of the holes for the middle meatus. Last, two more holes for the olfactory cleft were added on the anterior and posterior end of the cribriform plate. After creating the holes, the edited DICOM data were converted to STL format for 3D printing. The actual printed model consisted of three objects: a main body and two small parts, as shown in Figure 1b. These two parts were carved out to facilitate sensor insertion and realize reproducible measurements. The two small parts were detachable; they were removed during sensor insertion into the main body, then reattached and sealed with commercial plumbing putty to ensure an airtight measurement environment. The step to wash out unnecessary 3D printing remaining in the model took several days with extra care and was completed with endoscopic observation to ensure thorough removal.

2.2 | Measurement System and Procedure

The experimental setup was constructed to simulate physiological airflow under strictly controlled and reproducible conditions. The system consisted of several specialized units, including a pump, solenoid valves, flow meters, and a high-precision pressure differential sensor.

We employed a double-head type oil-less piston pump (100RND-ED, G&M Tech Inc.) because its flow rate range sufficiently covered typical human breathing levels. As shown in Figure 2a, the pump featured both suction and discharge ports, which were integrated with four direct-acting 2-port solenoid valves (FFB series, CKD Corporation). This configuration allowed us to mimic breathing cycles by alternating the flow direction; specifically, we programmed the system for a standard cycle of 5.0 s for inhalation and 5.0 s for exhalation. Furthermore, the system demonstrated the flexibility to replicate faster breathing patterns, such as 1.0 s inhalation and 1.5 s exhalation, or even rapid cycles as short as 0.2 s.

To capture the subtle aerodynamic changes within the model, we used a low-differential-pressure sensor (PSE550, SMC Corporation). This sensor was selected for its high precision (0.001 kPa accuracy), which was essential for the objectives of this study. Airflow rates were monitored using a 2-color display digital flow switch (PF2M7 series, SMC Corporation), which provided reliable measurements across the required flow range. All data were recorded via a data logger (USB-6002, Emerson Electric Co.) and controlled using LabVIEW software.

The pressure differential sensor was connected to a pipe via tubing, and the tip of this pipe was inserted into the model through the standardized holes (Figure 2b). A custom-built setup held the pipe securely to maintain a constant measurement depth. To ensure the integrity of the measurements, we conducted a pre-test by flowing air at each target rate (25, 30, 35, 40, and 45 L min⁻¹) and verifying that the flow meter readings remained stable and accurate, confirming the absence of any leakage. All unoccupied through-holes and nostrils were carefully plugged and sealed during the process.

2.3 | RM

To obtain a clinical baseline for each subject, active anterior RM was performed using a standard clinical rhinomanometer (MPR3100, NIHON KOHDEN). The measurements were conducted in accordance with established clinical guidelines and standard operating procedures [25]. The total nasal resistance was calculated at a reference pressure of 75 and 150 Pa. These global resistance values served as the reference standard for validating our 3D model-based local pressure measurements.

2.4 | Outcome Parameters

The primary outcome of this study was the local pressure differential (ΔP , Pa) measured at 12 anatomical locations (L1–L6 and R1–R6) to characterize regional airflow dynamics. The secondary outcome was the local nasal resistance (R , Pa/cm³/s), calculated

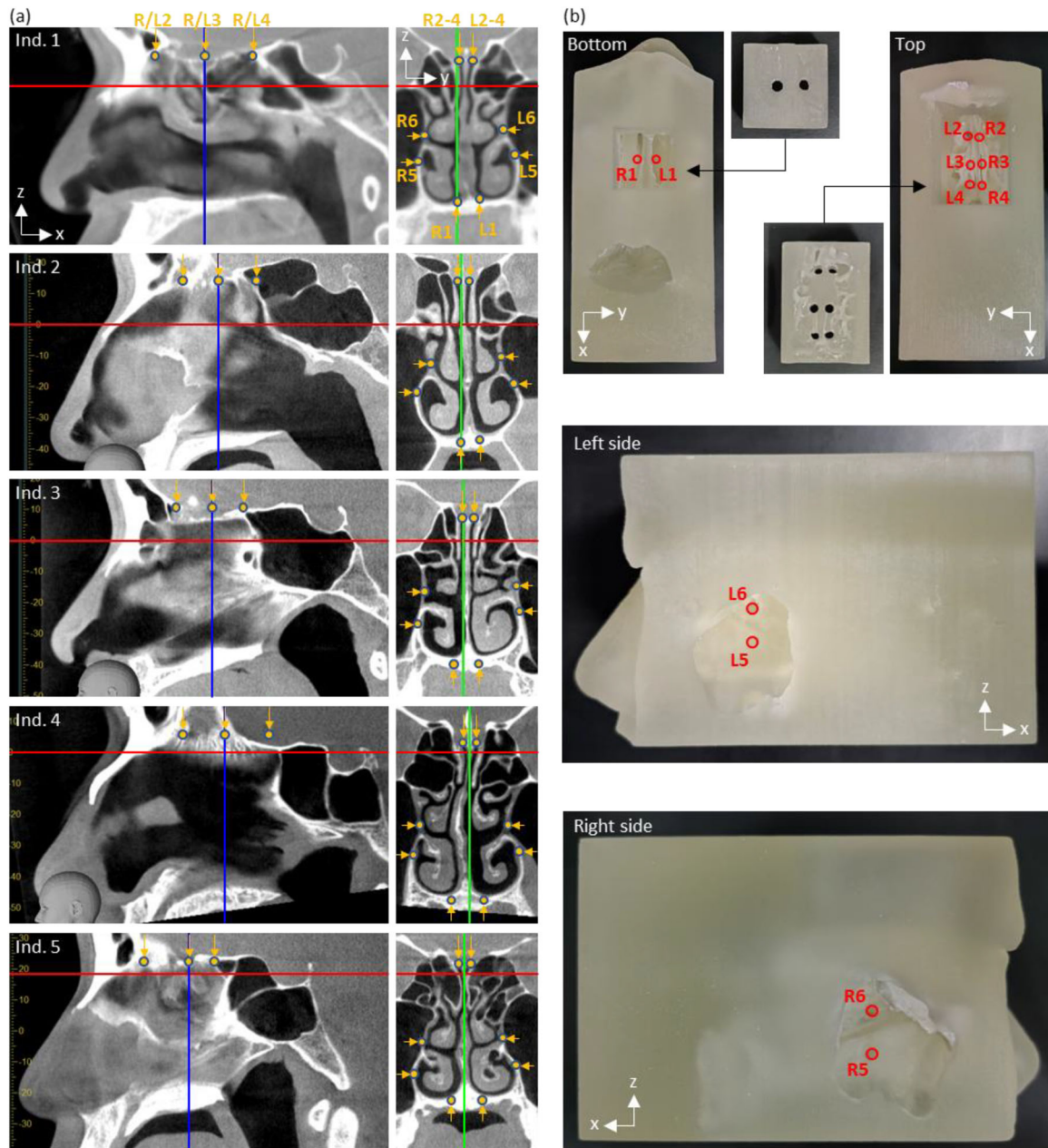


FIGURE 1 | Detailed structure of the 3D-printed nasal cavity model. (a) CT images of five individuals recruited for the present study. For each individual, sagittal and coronal CT images are shown side by side. The blue lines indicate the plane of the coronal section, while the green lines indicate the plane of the sagittal section. The exact positions where through-holes were created for the pressure measurements are indicated by orange dots and arrows in each image. (b) Photographs of the 3D-printed nasal cavity model taken from different directions. The model was fabricated as a three-part assembly: one main body (shown in the “Bottom” and “Top” views) and two detachable small parts (shown in the two smaller photographs between the “Bottom” and “Top” views). The small images of the two parts were included to show the internal contact surfaces that interface with the main body. The labels “Bottom” and “Top” denote the inferior and superior views of the main body, respectively. The positions for inserting a sensor for the pressure differential measurements are marked with red circles and labeled as L1–L6 for the left nasal cavity and R1–R6 for the right nasal cavity. Specifically, points 1 correspond to the nasal floor, 2–4 to the olfactory cleft, 5 to the inferior meatus, and 6 to the middle meatus.

using the standard formula: $R = \Delta P/V$, where V is the flow rate ($\text{cm}^3 \text{s}^{-1}$). Although nasal airflow is considered non-laminar even under quiet breathing conditions, this formula was used as the conventional physiological expression of nasal patency [26]. These parameters were used to evaluate the diagnostic resolution of our local measurement approach compared to conventional global rhinomanometry.

2.5 | Statistical Analysis

All pressure-differential data were obtained from five repeated measurement cycles at each flow rate to ensure reproducibility, and the results were presented as mean \pm standard deviation. To assess the uniqueness of the aerodynamic profiles for each subject, principal component analysis (PCA) was performed

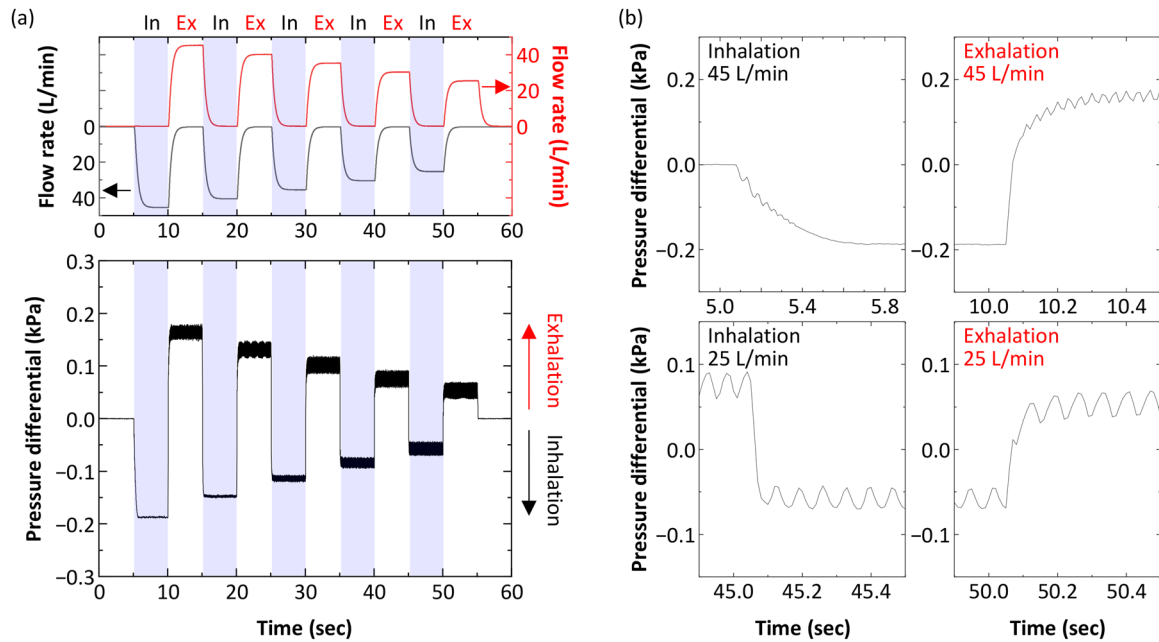


FIGURE 3 | Measured pressure differential under regularly switched inhalation/exhalation cycles. (a) Change in the pressure differential as a function of the flow rate. The flow rate profile was also recorded during the pressure differential measurement and is shown above the pressure differential data. (b) Zoom-in of the graph shown in (a). The transition between inhalation and exhalation at the minimum and maximum flow rates (25 and 45 L min⁻¹, respectively) was focused on to show the sensor response time.

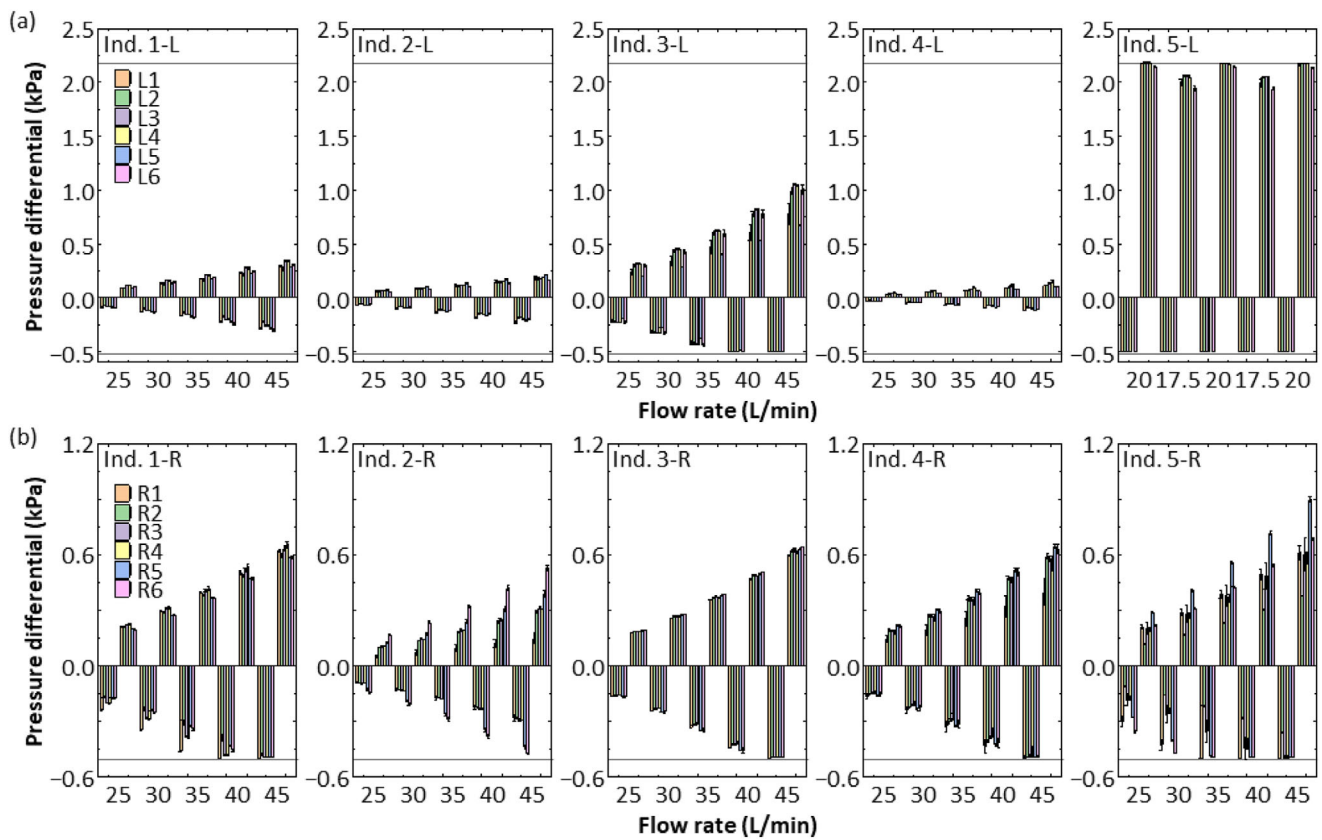


FIGURE 4 | Measured pressure differential data using five 3D-printed nasal cavity models. Position-dependent change in pressure differential as a function of flow rate: (a) left nose and (b) right nose. Note that the data for Ind. 5-L were recorded only at lower flow rates (17.5 and 20 L min⁻¹, measured repeatedly) than at other flow rates (25 to 45 L min⁻¹, measured sequentially). The dotted line represents the upper/lower limit of the pressure differential sensor used in this study. All error bars represent standard deviation.

TABLE 1 | Summary of subject profiles and clinical rhinomanometric data.

Subject ID	Age /gender	RM resistance [Pa/cm ³ /s]			
		Left		Right	
		75 Pa	150 Pa	75 Pa	150 Pa
Ind. 1	40s / Male	0.376	0.521	0.638	0.816
Ind. 2	60s / Male	0.358	0.417	0.455	0.546
Ind. 3	30s / Female	0.544	0.641	0.338	0.452
Ind. 4	40s / Male	0.278	0.407	0.487	0.588
Ind. 5	40s / Female	1.985	2.675	0.620	0.795

models. This allowed us to correlate our localized data with established global nasal resistance metrics.

3.2 | Comparison Between Model-Derived Resistance and Clinical RM

To validate our methodology against the clinical standard, we conducted a comparative analysis using the global resistance values obtained from RM. The clinical characteristics and the corresponding RM baseline for the five subjects are summarized in Table 1. All RM measurements exhibited typical S-shaped curves, as shown in Figure 5a. Following the international standards for RM [27], the pressure differential values at 75 and 150 Pa were used as representative reference points to evaluate nasal patency. These specific values correspond to flow conditions often observed prior to the onset of significant turbulence effects [28].

Following the outcome parameters defined in Section 2.4, we calculated R for both the RM data and our localized sensor measurements. Interestingly, the R values for both showed good agreement, especially for the right noses, regardless of the inconsistent flow rate range, as shown in Figure 5b,c. The left noses also showed similar trends; however, as the nasal resistance increased, a clear discrepancy emerged between the RM and sensor responses.

This divergence likely stemmed from differences in flow regimes within the complex nasal geometry, requiring Reynolds number (Re) estimation to understand the underlying fluid dynamics. Re is defined as

$$Re = \frac{\rho v L}{\mu} \quad (1)$$

where ρ is the density of air (kg m⁻³), v is the velocity of airflow (m s⁻¹), L is the characteristic length (m; the hydraulic diameter is usually used for the nasal cavity), and μ is the viscosity of air (Pa s). Since the nasal cavity structure is very complex, the transition from laminar to turbulent flow occurs with a lower Re number, even less than 1,000, compared to the transition in a pipe (approximately 2300) [29, 30]. Considering that typical nasal cavities have a hydraulic diameter of 1 cm or less [30], Re can easily exceed 1,000, indicating that the flow becomes more or less turbulent. To investigate this aerodynamic behavior at each

measurement site, we applied the power-law fitting (see Figures S2 and S3 for detailed plots) [25, 31–33]. The resulting fitting parameters—specifically the exponents (b)—provided critical insights into the local fluid dynamics. At most measurement sites, the b values consistently approached 2.0 (ranging from 1.8 to 2.1). This near-quadratic scaling aligned with the Rohrer model,

$$\Delta P = k_1 v + k_2 v^2 \quad (2)$$

where the quadratic term ($k_2 v^2$) represents the dominance of inertial or turbulent losses. The high b values observed in our study confirmed that the k_2 term was dominant under the present experimental conditions. Importantly, nasal resistance could dramatically increase in a remarkably narrow nasal structure, such as Ind. 5-L, leading to a large discrepancy in nasal resistance. These insights into flow dynamics, particularly in challenging cases like Ind. 5-L, reinforced the necessity for localized measurements and their improvements for a better understanding of these complicated phenomena.

3.3 | Subject Discrimination Using PCA

Another practical merit of localized measurements was that we could collect detailed person-specific information. Considering that RM provided a global nasal resistance that almost linearly increased in the representative measurement range of 75 and 150 Pa, the RM results included limited information about the measured persons regardless of flow rate (Figure 5d). In contrast, the position-wise measurements reported here offered richer information than the RM. Even if the averaged nasal resistance among the six positions was similar, such as in the case of the right nose (Figure 5c), the independent nasal resistance values from each position included unique information. Taking advantage of these non-linear characteristics, similar nasal structures were discriminated using PCA, as shown in Figure 5e). Thus, by collecting a large amount of data, including data from persons with a specific nasal disease, the present approach could lead to facile classification based on nasal conditions.

4 | Conclusion

We developed a facile, pressure-based approach to evaluate localized airflow dynamics within the nasal cavity using person-specific 3D-printed models. This method directly addressed the critical limitation of conventional RM, its inability to provide local structural details, by offering position-dependent pressure values. We demonstrated that nasal resistance estimated using our approach closely correlated with global resistance obtained using rhinomanometric measurements, thereby validating its utility while significantly enhancing the diagnostic resolution. Given that RM is used as a worldwide standard technique to evaluate nasal flow that reflects nasal conditions, such as the presence of obstructions or physical abnormalities, the present approach offered equivalent information with an easy and reproducible operation. Compared with an RM result that simply connected with the global resistance of the nasal cavity, the present approach provided an additional aspect of acquiring position-dependent pressure values, which allowed us to discuss the correlation between nasal flow and our olfactory ability in more detail. The

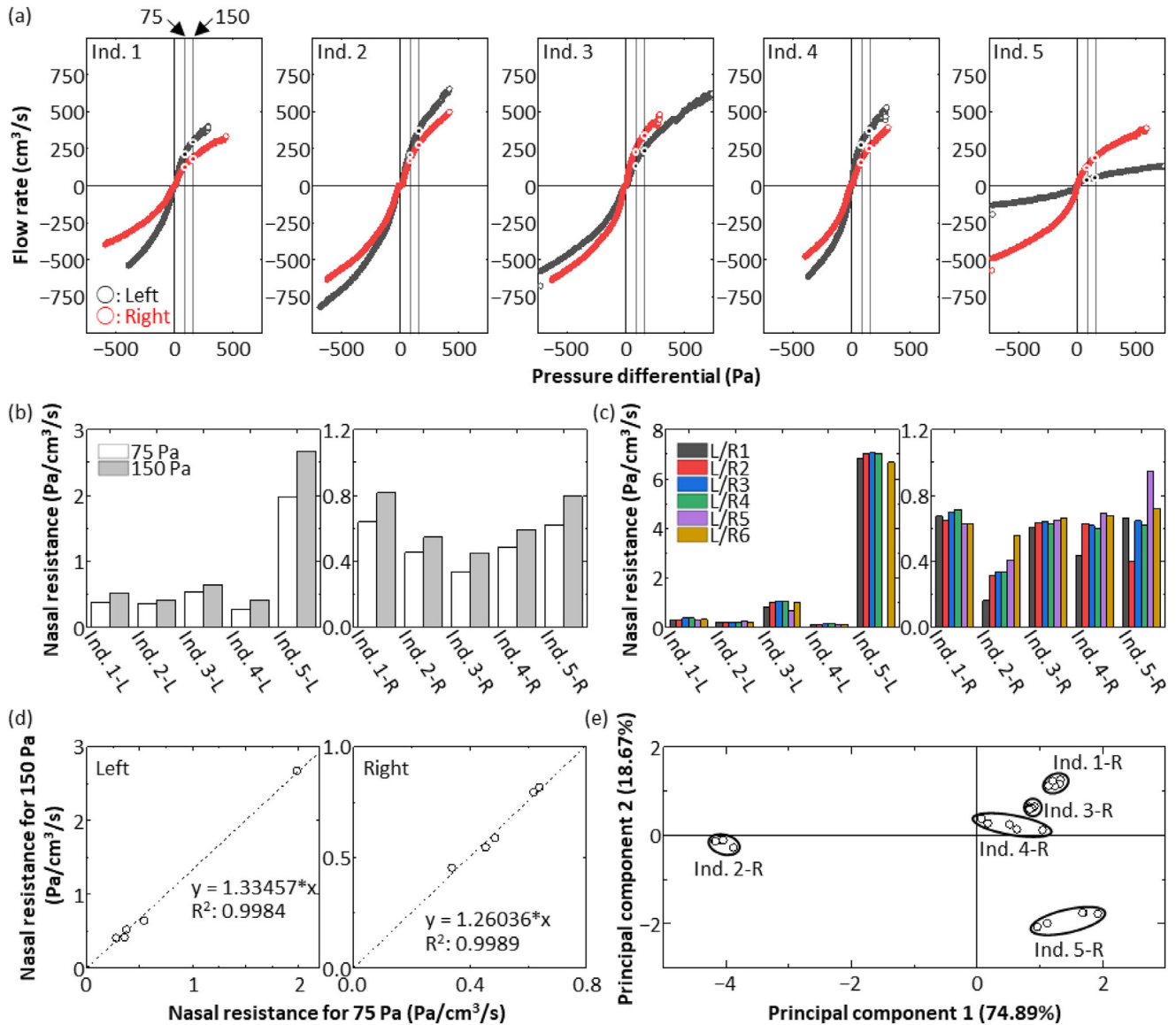


FIGURE 5 | Advantage of the present approach validated using conventional RM. (a) RM results measured using five 3D-printed nasal cavity models. (b, c) Nasal resistance-based comparison: (b) RM results obtained at 75 and 150 Pa, and (c) experimental data collected from the six positions. (d) Relationship between nasal resistance obtained at 75 and 150 Pa. The linear fitting results were also shown as dotted lines. (e) Principal component analysis based on the data collected from the right nostrils of the five individuals.

use of CFD and/or other relevant techniques will help further extend the possibility of applying the present approach in clinical situations, olfactory sensing, and understanding complex fluid flow.

Acknowledgments

This work was financially supported by a Grant-in-Aid for Scientific Research (B), JSPS, MEXT, Japan (No. 24K01520). The authors acknowledge the use of Gemini 3 (Google AI) for the conceptual design and partial generation of the Table of Contents figure.

Funding

This work was supported by a Grant-in-Aid for Scientific Research (B), JSPS, MEXT, Japan (No. 24K01520).

Ethics Statement

This study was approved by the Ethics Committee of the Jikei University School of Medicine (Approval No. 34–250[11402]). Informed consent was obtained from all participants prior to their inclusion in the study.

Conflicts of Interest

The authors declare no conflicts of interest.

Data Availability Statement

The data that support the findings of this study are available from the corresponding authors upon reasonable request.

References

1. E. H. C. Wong and R. Eccles, “Comparison of the Classic and Broms Methods of Rhinomanometry Using Model Noses,” *European Archives of Oto-Rhino-Laryngology* 272 (2015): 105–110.

2. E. H. C. Wong and R. Eccles, "Comparison of Classic and 4-Phase Rhinomanometry Methods, Is There Any Difference?," *Rhinology Journal* 52 (2014): 360–365.
3. H. L. Thulesius, A. Cervin, and M. Jessen, "Can We Always Trust Rhinomanometry?," *Rhinology Journal* 49 (2011): 46–52.
4. R. Eccles, "A Guide to Practical Aspects of Measurement of human Nasal Airflow by Rhinomanometry," *Rhinology Journal* 49 (2011): 2–10.
5. M. Atzori, G. D. Ciacchi, and M. Quadrio, "Understanding the Mismatch between In-Vivo and In-Silico Rhinomanometry," *Medical & Biological Engineering & Computing* 64 (2025): 219–229.
6. N. Schmidt, H. Behrbohm, L. Goubergrits, T. Hildebrandt, and J. Brüning, "Comparison of Rhinomanometric and Computational Fluid Dynamic Assessment of Nasal Resistance with Respect to Measurement Accuracy," *International Journal of Computer Assisted Radiology and Surgery* 17 (2022): 1519–1529.
7. G. B. Cherobin, R. L. Voegels, F. R. Pinna, E. M. M. S. Gebrim, R. S. Bailey, and G. J. M. Garcia, "Rhinomanometry versus Computational Fluid Dynamics: Correlated, but Different Techniques," *American Journal of Rhinology & Allergy* 35 (2021): 245–255.
8. M. Berger, A. I. Giotakis, M. Pillei, et al., "Agreement between Rhinomanometry and Computed Tomography-Based Computational Fluid Dynamics," *International Journal of Computer Assisted Radiology and Surgery* 16 (2021): 629–638.
9. N. Patil and S. Jain, "Rhinomanometry: a Comprehensive Review of Its Applications and Advancements in Rhinology Practice," *Cureus* 16 (2024): e61370.
10. K. Naito, S. Horibe, Y. Tanabe, H. Kato, S. Yoshioka, and I. Tateya, "Objective Assessment of Nasal Obstruction," *Fujita Medical Journal* 9 (2023): 53–64.
11. C. Li, A. A. Farag, G. Maza, et al., "Investigation of the Abnormal Nasal Aerodynamics and Trigeminal Functions among Empty Nose Syndrome Patients," *International Forum of Allergy & Rhinology* 8 (2018): 444–452.
12. A. Dayal, J. S. Rhee, and G. J. M. Garcia, "Impact of Middle versus Inferior Total Turbinatectomy on Nasal Aerodynamics," *Otolaryngology–Head and Neck Surgery* 155 (2016): 518–525.
13. G. L. Liu, W. J. Martin, Y. Mirmozaffari, R. Ni, and Z. Li, "Computational Modeling of Nasal Cavity Aerodynamics: Implications for Surgical Outcomes and Targeted Drug Administration," *Ear, Nose, & Throat Journal* 9 (2025): 1455613251335109.
14. H. Fatahi, A. Dastan, S. Sadrizadeh, and O. Abouali, "Numerical Study of Nasal Hair Effects on Breathing Comfort and Particle Deposition in a Simplified Vestibule Region," *Biomechanics and Modeling in Mechanobiology* 24 (2025): 1513–1533.
15. K. Bradshaw, P. Warfield-McAlpine, S. Vahaji, et al., "New Insights into the Breathing Physiology from Transient respiratory Nasal Simulation," *Physics of Fluids* 34 (2022): 14.
16. A. A. T. Borojeni, G. J. M. Garcia, M. G. Moghaddam, et al., "Normative Ranges of Nasal Airflow Variables in Healthy Adults," *International Journal of Computer Assisted Radiology and Surgery* 15 (2020): 87–98.
17. K. Zhao and J. B. Jiang, "What Is Normal Nasal Airflow? A Computational Study of 22 Healthy Adults," *International Forum of Allergy & Rhinology* 4 (2014): 435–446.
18. P. Niegodajew, "Flow Patterns and Vortex Formation Mechanisms inside a Human Nasal Cavity," *Physics of Fluids* 37 (2025): 19.
19. G. B. Cherobin, R. L. Voegels, E. M. M. S. Gebrim, and G. J. M. Garcia, "Sensitivity of Nasal Airflow Variables Computed via Computational Fluid Dynamics to the Computed Tomography Segmentation Threshold," *PLoS ONE* 13 (2018): e0207178.
20. S. Basu, D. O. Frank-Ito, and J. S. Kimbell, "On Computational Fluid Dynamics Models for Sinonasal Drug Transport: Relevance of Nozzle Subtraction and Nasal Vestibular Dilation," *International Journal for Numerical Methods in Biomedical Engineering* 34 (2018): e2946.
21. S. G. Johnsen, "Computational Rhinology: Unraveling Discrepancies between In Silico and In Vivo Nasal Airflow Assessments for Enhanced Clinical Decision Support," *Bioengineering-Basel* 11 (2024): 82.
22. C. Li, J. Jiang, H. Dong, and K. Zhao, "Computational Modeling and Validation of Human Nasal Airflow under Various Breathing Conditions," *Journal of Biomechanics* 64 (2017): 59–68.
23. R. H. J. Hebbink, B. J. Wessels, R. Hagmeijer, and K. Jain, "Computational Analysis of human Upper Airway Aerodynamics," *Medical & Biological Engineering & Computing* 61 (2023): 541–553.
24. J. Van Strien, K. Shrestha, S. Gabriel, et al., "Pressure Distribution and Flow Dynamics in a Nasal Airway Using a Scale Resolving Simulation," *Physics of Fluids* 33 (2021): 14.
25. P. A. Clement and F. Gordts, "Consensus Report on Acoustic Rhinometry and Rhinomanometry," *Rhinology* 43 (2005): 169–179.
26. K. Naito, S. Horibe, Y. Tanabe, H. Kato, S. Yoshioka, and I. Tateya, "Objective Assessment of Nasal Obstruction," *Fujita Medical Journal* 9 (2023): 53–64.
27. P. A. Clement, "Committee Report on Standardization of Rhinomanometry," *Rhinology* 22 (1984): 151–155.
28. J. R. Wheatley, T. C. Amis, and L. A. Engel, "Nasal and Oral Airway Pressure-Flow Relationships," *Journal of Applied Physiology* 71 (1991): 2317–2324.
29. D. J. Doorly, D. J. Taylor, and R. C. Schroter, "Mechanics of Airflow in the human Nasal Airways," *Respiratory Physiology & Neurobiology* 163 (2008): 100–110.
30. K. Keyhani, P. W. Scherer, and M. M. Mozell, "Numerical Simulation of Airflow in the Human Nasal Cavity," *Journal of Biomechanical Engineering* 117 (1995): 429–441.
31. P. Broms, B. Jonson, and C. J. Lamm, "Rhinomanometry. Rhinomanometry. II. A System for Numerical Description of Nasal Airway Resistance," *Acta Oto-Laryngologica* 94 (1982): 157–168.
32. D. W. Cockcroft, D. W. MacCormack, S. M. Tarlo, F. E. Hargreave, and L. D. Pengelly, "Nasal Airway Inspiratory Resistance," *American Review of Respiratory Disease* 119 (1979): 921–926.
33. J. Pfitzner, "Poiseuille and His Law," *Anaesthesia* 31 (1976): 273–275.

Supporting Information

Additional supporting information can be found online in the Supporting Information section.

Supporting File: adrs70162-sup-0001-SuppMat.docx.